Remote Sens. **2015**, *7*, 8516-8542; doi:10.3390/rs70708516

OPEN ACCESS

remote sensing

ISSN 2072-4292

www.mdpi.com/journal/remotesensing

Article

Remote Sensing of River Delta Inundation: Exploiting the Potential of Coarse Spatial Resolution, Temporally-Dense MODIS Time Series

Claudia Kuenzer [1,*], Igor Klein [1], Tobias Ullmann [2], Efi Foufoula Georgiou [3], Roland Baumhauer [2] and Stefan Dech [1,2]

[1] German Remote Sensing Data Centre, DFD, German Earth Observation Center, EOC, of the German Aerospace Centre, DLR, Oberpfaffenhofen, D-82234 Wessling, Germany; E-Mails: igor.klein@dlr.de (I.K.); stefan.dech@dlr.de (S.D.)

[2] Department of Geography and Geology, University of Wuerzburg, Am Hubland, D-97074 Wuerzburg, Germany; E-Mails: tobias.ullmann@uni-wuerzburg.de (T.U.); baumhauer@uni-wuerzburg.de (R.B.)

[3] Department of Civil Engineering, University of Minnesota, Twin Cities, St. Anthony Falls Laboratory & National Center for Earth-surface Dynamics (NCED), 2 Third Avenue SE, Minneapolis, MN 55414, USA; E-Mail: efi@umn.edu

* Author to whom correspondence should be addressed; E-Mail: claudia.kuenzer@dlr.de; Tel.: +49-8153-28-3280; Fax: +49-8153-28-1458.

Academic Editors: Deepak R. Mishra and Prasad S. Thenkabail

Received: 9 April 2015 / Accepted: 17 June 2015 / Published: 6 July 2015

Abstract: River deltas belong to the most densely settled places on earth. Although they only account for 5% of the global land surface, over 550 million people live in deltas. These preferred livelihood locations, which feature flat terrain, fertile alluvial soils, access to fluvial and marine resources, a rich wetland biodiversity and other advantages are, however, threatened by numerous internal and external processes. Socio-economic development, urbanization, climate change induced sea level rise, as well as flood pulse changes due to upstream water diversion all lead to changes in these highly dynamic systems. A thorough understanding of a river delta's general setting and intra-annual as well as long-term dynamic is therefore crucial for an informed management of natural resources. Here, remote sensing can play a key role in analyzing and monitoring these vast areas at a global scale. The goal of this study is to demonstrate the potential of intra-annual time series analyses at dense temporal, but coarse spatial resolution for inundation characterization in five river deltas located in four different countries. Based on 250 m

MODIS reflectance data we analyze inundation dynamics in four densely populated Asian river deltas—namely the Yellow River Delta (China), the Mekong Delta (Vietnam), the Irrawaddy Delta (Myanmar), and the Ganges-Brahmaputra (Bangladesh, India)—as well as one very contrasting delta: the nearly uninhabited polar Mackenzie Delta Region in northwestern Canada for the complete time span of one year (2013). A complex processing chain of water surface derivation on a daily basis allows the generation of intra-annual time series, which indicate inundation duration in each of the deltas. Our analyses depict distinct inundation patterns within each of the deltas, which can be attributed to processes such as overland flooding, irrigation agriculture, aquaculture, or snowmelt and thermokarst processes. Clear differences between mid-latitude, subtropical, and polar deltas are illustrated, and the advantages and limitations of the approach for inundation derivation are discussed.

Keywords: remote sensing; river deltas; inundation; flooding; MODIS; Yellow River Delta; Mekong Delta; Irrawaddy Delta; Ganges-Brahmaputra Delta; Mackenzie Delta

1. Introduction: Background and Scope of This Paper

In recent decades numerous studies have dealt with the derivation of inland water surfaces from remote sensing data [1]. Depending on the thematic focus of the respective study, terms such as "water body derivation" [2], "flood mapping" [3–5], or "inundation monitoring" [6–9] have been used. Whereas the wording "water body" derivation is usually used when dealing with inland lakes or ponds, or any permanent water body (also reservoirs, *etc.*), the term "flood" mapping or monitoring is usually used when natural hazard events are being observed. Earth observation based flood mapping aims at the delineation of affected areas that are not usually water covered under average conditions [10], and furthermore at damage assessment during flood situations along major rivers, also after storm surges and catastrophic events such as tsunamis [11]. The term "inundation analysis" or "inundation mapping" is usually used in regions where water surfaces exhibit high spatio-temporal dynamics without a catastrophic or destructive character. Typically, inundation analyses are performed for the world's untamed river ecosystems, major wetlands, and inland as well as coastal river deltas [12–16].

Remote sensing based water, flood, and inundation mapping can be based on either optical data or radar data, whereas the latter approach has the advantage that radar sensors are active sensors, pulsing a radar beam to the earth's surface, and registering the backscattered signal at a receiving unit. Therefore, radar and synthetic aperture radar (SAR) based data collection can be performed during day and night [17]. Furthermore, the pulsed microwaves can penetrate clouds and haze that commonly exist during rainy seasons or weather situations that cause floods [17]. Hence, SAR data have been the preferred choice for water, flood, and inundation mapping activities [18,19]. Research based on data from SAR sensors onboard satellites such as the Canadian Radarsat-1 and -2, the European ENVISAT (Environmental Satellite) ASAR (Advanced Synthetic Aperture Radar), the Japanese Advanced Land Observing Satellite (ALOS) Palsar sensor, the Italian COSMO-Skymed (Constellation of small Satellites for Mediterranean basin Observation) and the German TerraSAR-X has well demonstrated the potential of this sensor type [20–23].

The great disadvantage of SAR data is that they are usually not easily accessible for large areas [24]. Radarsat data for large areas have to be purchased, and the same holds true for COSMO-Skymed and TerraSAR-X data, which are only available for scientific studies at limited spatial extent. Although the free ENVISAT ASAR archives provide SAR data for large areas, the sensor failed in April 2012. Thus, no recent ENVISAT ASAR data are available. In early 2014 the European Space Agency ESA launched the novel Sentinel-1 sensor, which will most likely become the major workhorse for SAR based studies [24], but global scale data are not yet available to the scientific community. Due to the access limitations of SAR several authors have also considered coarse to high resolution optical data for water surface mapping [25–28]. Although optical sensors cannot acquire imagery during clouded conditions, coarse resolution sensors such as the Moderate Resolution Imaging Spectroradiometer, MODIS, offer the advantage of daily data acquisition. The MODIS sensor flown on the Terra and Aqua platforms even covers each spot on the earth's surface—except the polar regions—up to four times per diurnal cycle—at least two observations during daylight are thus possible. Several authors have used MODIS data of 250 m spatial resolution to map water bodies, floods, and inundation dynamics [27,29]. The dense temporal sampling interval of MODIS provides the opportunity for the generation of annual time series with daily coverage. Filtering and compositing approaches allow the removal of clouds from the time series and thus the generation of daily thematic products [30].

In this paper we reveal the inundation characteristics of five selected river deltas covering different countries and continents, based on generating and exploiting an intra-annual time series of 250 m MODIS data. River deltas are among the most densely populated places on earth. Although deltas only cover about 5% of the global land mass, between 500 to 600 million people live there. Delta assets include a flat topography, which eases settlement and economic development, access to sea water, fresh water, fluvial and marine resources, and opportunities for ice-free harbours and transport connections into the hinterland of a river basin. Deltas are often home to underground reserves of oil and gas, and/or salts. Rich wetland flora and fauna biodiversity is common [31–34]. We selected the four densely populated river delta areas of the Yellow River Delta, China, the Mekong Delta in Vietnam, the Irrawaddy Delta in Myanmar, the Ganges-Brahmaputra Delta in India and Bangladesh, as well as in contrast, the nearly uninhabited polar Mackenzie River Delta Region in northwestern Canada as study sites to reveal patterns of inundation and the respective drivers. Questions addressed at the respective observation scale include:

- Does inundation occur on the land surface in the respective deltas?
- Which area and which percentage of the river delta is affected by inundation and what is driving these inundation patterns?
- How often are certain areas inundated, and does rare or long-term inundation prevail?
- What are the advantages and disadvantages of coarse resolution optical data for inundation mapping?

We use the term "inundation" throughout the paper, as this indicates that a surface area is water covered without the notion of a (usually negative) flood. Inundated areas can be natural permanent water surfaces, inundated (e.g., irrigated) fields, other managed land (e.g., aquaculture *etc.*), as well as large scale flooded land.

2. Study Areas and Data

The Yellow River Delta, located in China's Shandong Province, is the delta of China's second longest river, which has the highest erosion rate globally [35,36]. The larger delta spans an area of 10,000 km^2 (the delta core area of about 4000 km^2) and about six million people live in Dongying district, the main delta area. The Yellow River Delta is part of Shengli oil field, which is China's second largest oil field with extensive ongoing exploration activities. At the same time the delta is home to two large nature reserves that host a rich biodiversity and were declared Ramsar wetland sites in 2013. Ongoing land use change is dominated by industrial and urban sprawl, the expansion of aquaculture areas, and increased harnessing of the coast via dykes and levees [32,37–39].

The Mekong Delta is an area of 39,000 km^2 where the Mekong splits up into nine arms draining into the South China Sea. Some 17 million inhabitants live in the delta, which is often termed the "rice bowl" of Southeast Asia. It is an important food base for Vietnam; 50% of that country's nationally consumed rice, 60% of its nationally consumed fruits, and 60% of its fish and seafood are produced there. The delta landscape is characterized by a complex network of natural and man-made waterways and canals, large rice paddy fields, fruit tree orchards, aquaculture dominated coastal zones, and decreasing mangrove forests along the coasts. The largest city in the delta is Can Tho with about 1.5 million inhabitants—but overall the delta resembles a rural landscape [15,16,31,40–43].

The Irrawaddy Delta is Myanmar's lowest lying land expanse, where the silt-laden Irrawaddy River splits off into several arms and flows into the Bay of Bengal. It covers about 40,000 km^2. The river mouth area at the coast extends for over 130 km from east to west. The delta is framed by the hilly ranges of Rakhine Yoma in the west and Bago Yoma in the east. The humid, monsoonal region is densely populated (1000 persons/km^2). About 3.5 million inhabitants live in fishing and farming communities. Rice is grown on the fertile delta plains, which are all less than 3 m above sea level. Despite over 1000 km of embankments to protect the rice paddy fields, the delta does not have a man-made network of waterways and canals in contrast to the Mekong. Mangrove and Nypa palms characterize the natural vegetation [44].

The Ganges Brahmaputra Delta is the largest river delta in the world, covering nearly 80,000 km^2. It stretches from the Hooghly River in the west to the Meghna River in the east along the coast at the Bay of Bengal. The Padma and Jamuna rivers join north of the delta and are in turn joined by the Meghna River before entering the Indian Ocean. Two thirds of the delta belong to Bangladesh, one third to India. The delta is one of the most fertile regions globally. Over 143 million people live there. Jute, tea, and rice are the major crops, and fishing secures the inhabitants' protein supply [45].

The Mackenzie Delta Region in northwestern Canada belongs to the Northern Beaufort Continental Shelf bordering the Arctic Ocean. It is the second largest delta of the polar zone. In these arctic latitudes dominated by continuous permafrost no agriculture or land management takes place. Only some selected (and recently expanding) oil and gas extraction activities disturb the otherwise untouched environment. About 40%–50% of the delta's alluvial land is covered with small lakes (about 49,000) and rivers. Lakes are shallow and mostly result from thermokarst processes [46].

Table 1 presents the quantitative facts about the five study areas. Additionally to being remote sensing scientists, all authors of this paper have in-depth and long-term *in-situ* knowledge of one or several of the river deltas addressed.

Table 1. Overview of the five river delta areas addressed in this study.

Delta	Country	Area	Population	Climate (Köppen-Geiger)
Yellow River Delta	China	10,000 km^2	6,000,000	Snow, winter dry, hot summer (Dwa)
Mekong Delta	Vietnam	39,000 km^2	17,000,000	Equatorial-monsoonal (Am)
Irrawaddy Delta	Myanmar	40,000 km^2	3,500,000	Equatorial-monsoonal (Am)
Ganges-Brahmaputra Delta	India/Bangladesh	80,000 km^2	143,000,000	Equatorial-monsoonal, winter dry (Am, Aw)
Mackenzie Delta	Canada		< 10,000	Polar tundra (ET)

Although there are several global water body data sets available, such as the Shuttle Radar Topography Mission (SRTM) water body data (SWBD) [47], the Global Lakes and Wetlands Data (GLWD) [48], the latest 250 m MODIS water mask [49], and the new high spatial resolution Global Water Bodies (GLOWABO) data set [50], all of them are static products, representing a status at a certain point or period in time, but not allowing analyses of inundation or water body dynamics. As our goal was to generate cloud-free water/non-water products (termed water masks in the following) with the highest possible (daily) temporal resolution, our analyses were based on available near infrared (NIR) MODIS reflectance data acquired daily from the Terra and Aqua platforms. To analyse annual inundation patterns, a complete year of data for all five study areas (six MODIS tiles, as the Mekong Delta is covered by two tiles) had to be processed and analysed. The main data source for the analyses was daily near infrared (NIR) reflectance values from MOD09GQ and MYD09GQ with a spatial resolution of 250 m. These data sets are distributed as gridded level 2 geocorrected (L2G) products providing atmospherically-corrected surface reflectance values at 620–670 nm (band 1) and 841–876 nm (band 2) [51,52]. Tiles h28v07+h28v08 (Mekong Delta), h27v05 (Yellow River Delta), h27v07 (Irrawaddy Delta), h26v06 (Ganges Brahmaputra Delta), and h13v02 (Mackenzie Delta Region) were downloaded. This means that, for each of the five study areas, all available daily scenes—4380 tiles overall (two scenes per study area, six scenes, 365 days)—had to be processed. Additionally, the 500 m resolution snow cover products MOD10A1 and MYD10A1, containing thematic information such as daily cloud coverage and snow coverage, as well as static information on oceans and inland lakes [53], and the static water mask MOD44W with a spatial resolution of 250 m [49] were employed in the process elucidated below. Digital elevation information at 90 m resolution, which has been generated from SRTM (Shuttle Radar Topography Mission) data and which was partially filled by digital elevation data from auxiliary DEMs and other sources, such as the USA-NED3 DEM, a Mexico 90m DEM, Canadian Digital Elevation Data Level 1, a 100m resolved DEM for New Zealand, Australian GEODATA TOPO 100k, a Costa Rican 50m DEM, an Ecuadorian 90m DEM, amongst others [54] was also available.

3. Method Applied for Inundation Derivation Based on MODIS Time Series Data

The approach used to derive water from the MOD09GQ and MYD09GQ data sets (see Figure 1) is based on the fact that water surfaces have a very low reflection in the NIR (band 2), which has been exploited by numerous authors performing single band based water mapping [55–62]. Due to the large amount of data (also aiming at processing larger areas covering many years) a single-band slicing method was also the preferred choice in this study—however, employing a dynamic reflectance

threshold calculation for each tile on each day. The master resolution of 250 m was defined by the MOD09GQ and MYD09GQ data sets, which were the main source for deriving water surfaces. Thus, the MOD10A1 and MYD10A1 data were up-sampled to this resolution and the SRTM+ data (and the derived slope layer), were down-sampled to this resolution, respectively. The data processing flow applied to all data of the year 2013 is depicted in Figure 1. Most important is the dynamic water thresholding, as the spectral characteristics of water bodies and inundated areas can vary with place and over time, which makes water/non-water distinction difficult. Differences in chlorophyll content, sediment load, surface roughness, and water depth can all influence the appearance of one and the same water surface in satellite imagery. Furthermore, the differing effectiveness of atmospheric correction can lead to varying reflectances even during similar on-ground conditions [63].

The extraction of water surfaces is based on the automatic extraction of training pixels from the MOD09GQ and MYD09GQ data sets, whose extent we defined by the MOD44W static water mask, while ensuring by means of the MOD10A1 and MYD10A1 product (containing cloud information) that no cloud-covered, ice-covered, snow-covered, or no-data pixels are extracted as training pixels. Furthermore, no pixels with a reflectance >20% in the NIR are allowed as training pixels. This ensures that no training data are generated in areas which might have been inundated during the MOD44W product generation but resembled land surfaces at the time of analysis. Mean and standard deviations of training pixel clusters [62,64] are then calculated based on the extracted training data set, and the reflectance value of the mean plus one standard deviation is defined as the threshold for water extraction, accounting for the above mentioned possible variability of water surfaces. Combining the Terra (MOD) and Aqua (MYD) derived water pixels for the same day then results in one water/ no-water mask for each day. Misclassifications of water can occur in shadowed steep terrain, where the reflectance in the NIR is low. However, this effect can be compensated with DEM-based post processing: wetlands and water bodies are usually not located on steeply sloped terrain, so that—based on the finding of Niu *et al.* [65]—one can mask out all areas with a slope steeper than 5° as possible inundated areas. Another source of misclassification are clouds and single scattered dark cloud shadows. This challenge can be overcome assuming that no cloud or cloud shadow will persist over an area for very long. Thus, a temporal filter was applied to exclude areas, which are affected by any of the two. A temporal filter of nine cells (four days before and four days after the observation) has been selected. Pixels which might resemble water surfaces but are flagged as clouds are filled with water or no-water information based on the temporally closest clear sky observation. The refined, daily water/no-water products are then summed up for one year to retrieve a water cover product ranging from 0 to 365 (days per year of water coverage) [62]. Overall, for the five deltas analyzed, six MODIS tiles had to be processed, and as two data sets per day and tile were processed, overall 4380 tile were processed to generate the intra-annual time series for the year 2013. As elucidated in Figure 1a “water mask” is derived for each day from the NIR reflectance bands, which allows to “stack 365 binary products and in this way generate an inundation frequency product ranging from 0 to 365 days of water coverage.

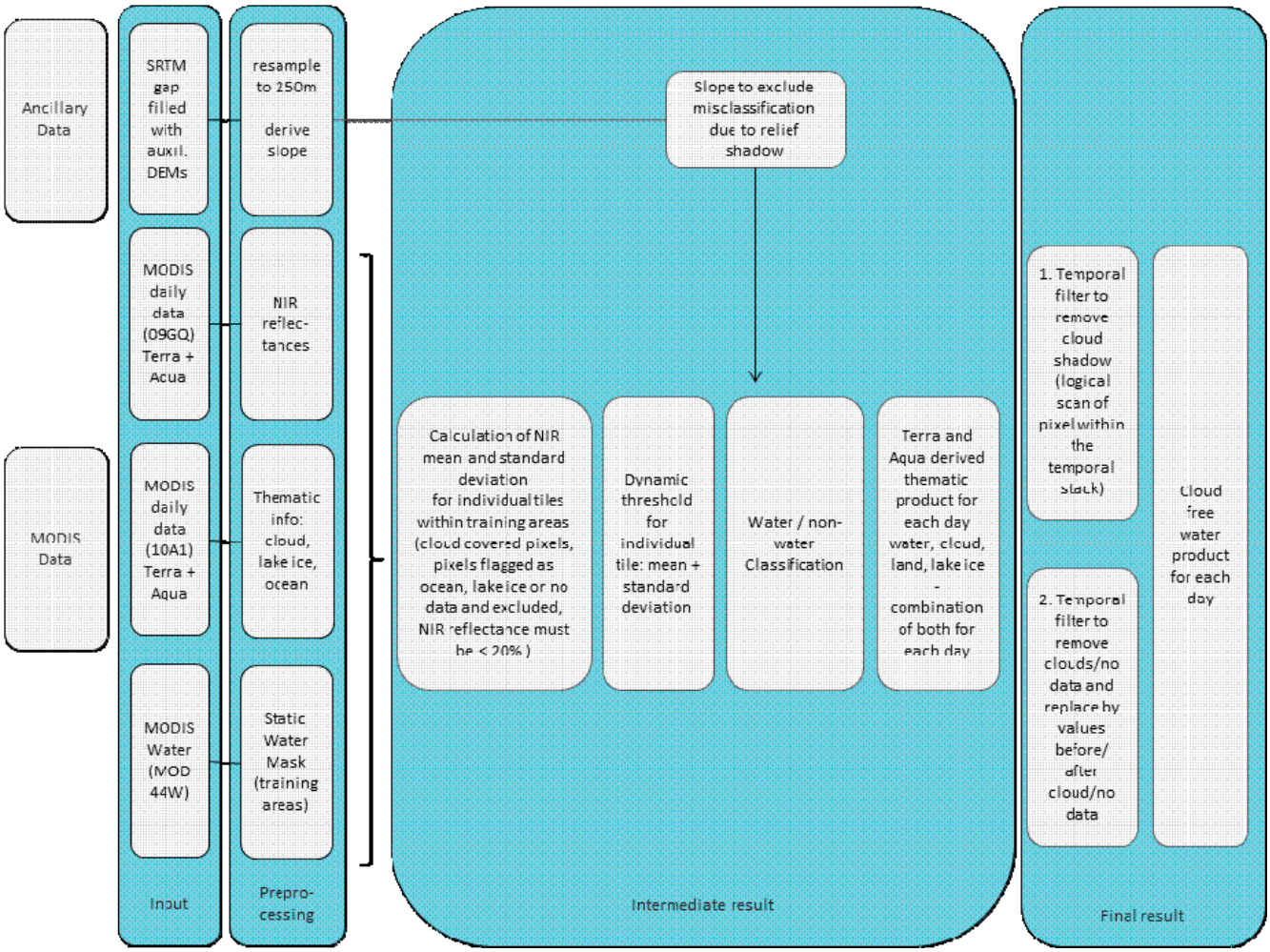

Figure 1. Processing chain of MODIS data and ancillary data for deriving intra-annual inundation information at 250 m spatial resolution, as undertaken for the complete year 2013.

4. Results

The results of data analysis for the five selected study areas are presented in Figures 2–6 and in summarizing Table 1. The information product depicting intra-annual inundation patterns is a product ranging from 0 to 365 days (from never inundated displayed in white, one time inundated displayed in red, up to inundated every day, displayed in dark blue, see Figure 2a), overlain on the gap-filled shaded digital elevation model, DEM, derived based on data of the Shuttle Radar Topography Mission, SRTM, and auxiliary DEM data. As terrain in river delta areas is usually not too accentuated, the DEM easily reveals regions with major terrain features. The information product depicting inundation patterns and duration (see Figure 2a) is always paired with a general satellite image overview of the respective area (see Figure 2b, source: Google Earth). Furthermore, for each river delta investigated, charts presenting the percentage and areal coverage (in km^2) of inundation duration (in days per year of the year 2013) in the respective delta are displayed (in a continuous manner: left diagram, as well as in a classified way: right diagram, see Figure 2c,d). In both diagrams the logarithmic scale of the two y-axes should be noted. It should be mentioned that the authors have in-depth field knowledge based on several years of field campaigns in the respective areas, and that they published further articles on the river deltas addressed. This allows for an interpretation and partial validation of the patterns observed.

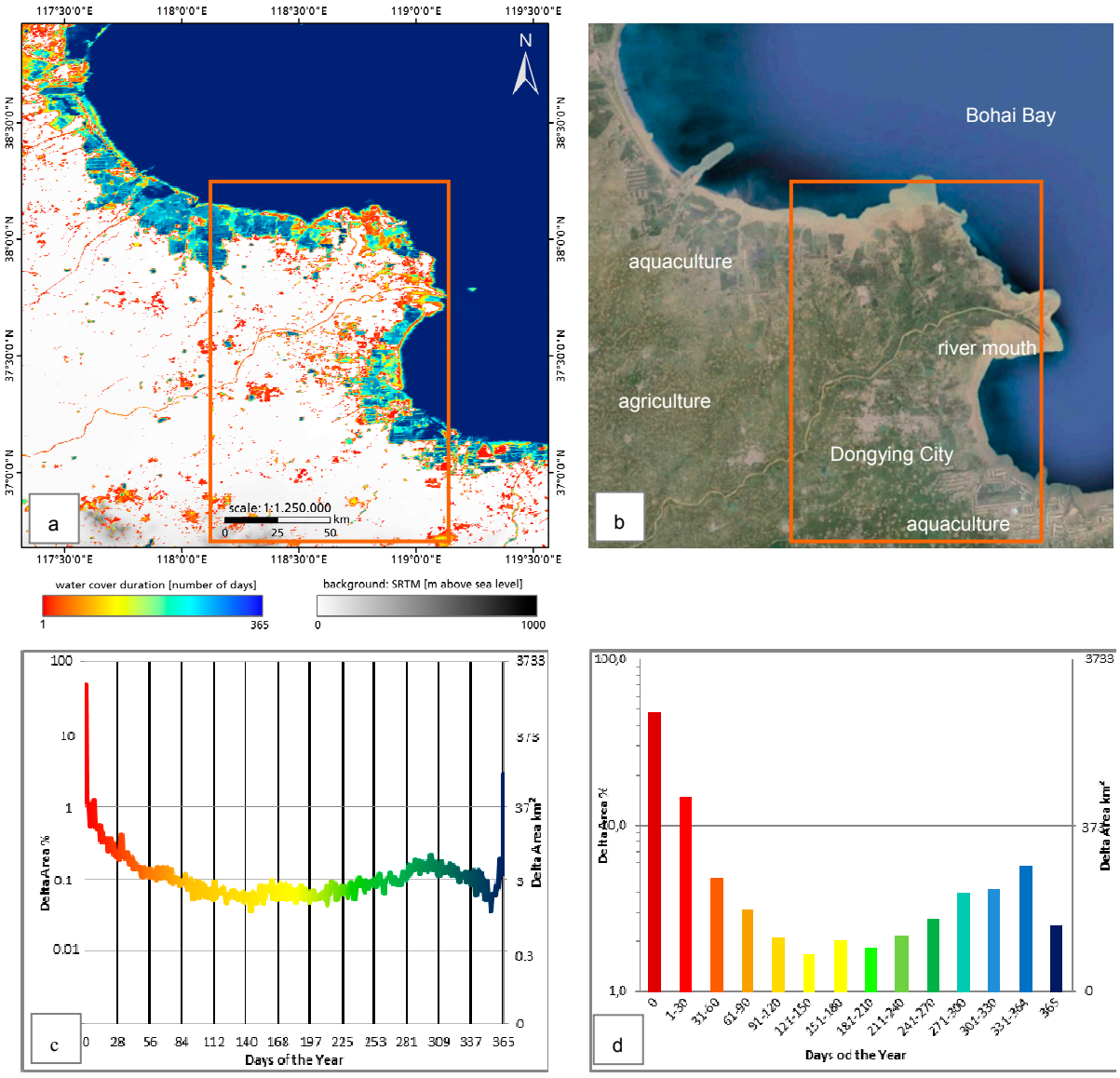

Figure 2. Intra-annual inundation patterns of the Yellow River Delta, China, derived from an annual time series of daily temporal resolution for the year 2013. Orange subset indicates validation area presented in Figure 3. (**a**) intra-annual inundation dynamics, (**b**) optical data for comparison, (**c**) and (**d**) quantitative analyses of inundation dynamics

Figure 2a depicts the intra-annual inundation patterns and distribution of the Yellow River Delta. It can be seen that inundation mostly occurs close to the coast, whereas inundation in the hinterland is not very prominent. In the hinterland one can observe inundation only in a few places: either as dark blue permanent small water bodies (water storage reservoirs, small lakes *etc.*), or as rarely inundated areas (reddish to yellowish tones) due to irrigation or water-logged areas after heavy rains. Along the coastline, a large accumulation of near-permanent water bodies is evident. These are aquaculture ponds (Figure 2b), which are inundated year-round (except for a few days or weeks for cleaning or re-construction) and which appear in darker bluish tones, whereas some salt farming (brine pond) areas appear in tones of lighter blue (not inundated as often as aquaculture areas) (see also Figure 3).

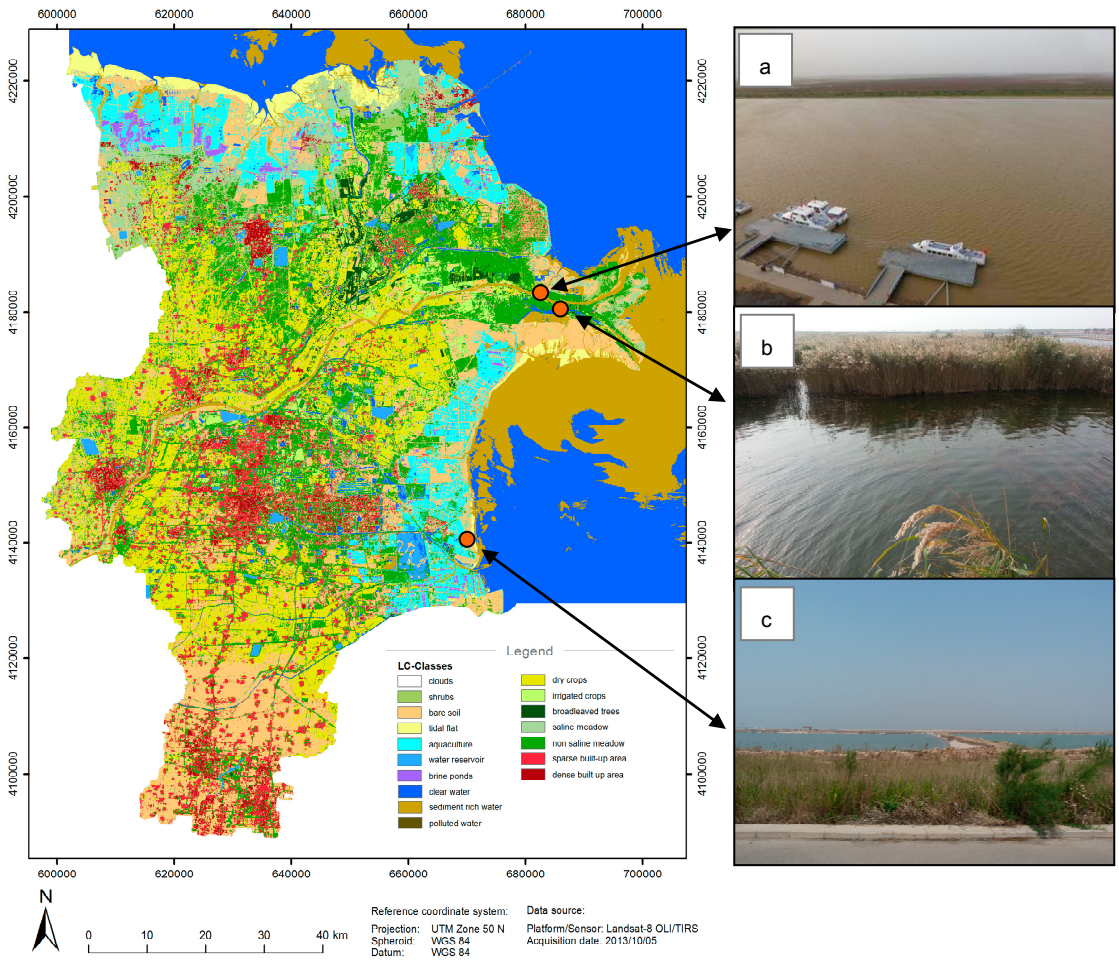

Figure 3. Landsat-8 derived land use classification for 2013 (kindly provided by M. Ottinger), as well as field photographs from 2013. (**a**) Yellow River mouth area; (**b**) wetlands; (**c**) aquaculture.

It is striking that the Yellow River itself does not show as a linear feature indicating water cover 365 times per year (which should be the case) (Figure 2a). The Yellow River has a very unusual spectral signature compared to the other rivers studied. The Yellow River's spectral signature often resembles a spectrum suggesting a mixture of water and soil (see Figure 3, upper photograph), and therefore reflectance in the near infrared is much higher than for clear water surfaces. Therefore, it can usually not be identified using a threshold designed to extract water surfaces from the complete MODIS tile. The field photographs (Figure 3) depict the challenges with water extraction in the Yellow River Delta environment—a region, where water color varies greatly due to varying sediment load. The Yellow River is not a feature existing in the MOD44W static water mask and therefore our approach does not consider training pixels in the river area (which is understandable, a river usually is much too narrow to allow as a good training site, especially if using 250 m resolved coarse resolution data). The water surface training samples in the area of the Yellow River Deltas thus stem from the few permanent water bodies in this region (such as wetland lakes, large storage reservoirs, and partially aquaculture)—all water surfaces, which are much clearer than the river itself (see Figure 3b,c). Thus, it is not striking that the river is not extracted as a permanent 365 day feature in Figure 2a.

Overall, 48.6% (1813 km^2) of the Yellow River Delta is never affected by inundation, whereas 15% (556 km^2) is water covered from one to 30 days. All other classes (31–60 days, 61–90 days, and so on) represent 1.8% to up to 6% of the delta. Regions which are always water covered/inundated sum up to 8.4% (309 km^2) of the overall delta area when considering all pixels water covered more than 331 days, or 2.5% (94 km^2) of the delta area when only considering pixels which are fully water covered for

365 days (Figure 2c,d). The overall inundation patterns coincide well with higher resolution inundation patterns derived from 30 m multispectral Landsat data presented by [39], studies exploiting SAR data time series for the Yellow River Delta, as presented by Kuenzer *et al*. [14], as well as a Landsat-8 data derived land use classification for 2013, presented in Figure 3 below. Aquaculture areas presented in Figure 2 coincide for over 88% with the most frequently inundated near-coastal water-bodies presented in Figure 3. From Ottinger *et al*. (2013) [39] and Kuenzer *et al*. [14] it is known that aquaculture is expanding rapidly in the region. The processing of several years of intra-annual inundation time series holds a great potential to observe and quantify this process for this large delta area.

A completely different pattern can be noted for the river delta of the Mekong. Compared to the Yellow River, it is striking that the river branches of the Mekong can clearly be noted as dark blue features in the inundation Figure 4a (water covered 365 days). In contrast to the Yellow River, which does not clearly show in Figure 3a, this has two reasons. Firstly, the river distributaries of the Mekong are—close to the river mouth—much wider than the main stem of the Yellow River. They can therefore be picked up easier in MODIS imagery of 250 m resolution. Secondly, the Mekong waters—while also rich in sediment—are less influenced by sediment spectral signatures than the much more sediment-laden Yellow River waters. Narrow canals dissecting the delta (see also Figure 5b cannot be extracted based on the MODIS data). The southwestern tip of the Mekong Delta contains large areas experiencing very long, up to year-round inundation (Figure 4a). These are aquaculture areas in the provinces of Ca Mau and Kien Giang, which have expanded at a rapid pace in recent years. Regions with a long inundation period of over 250 days along the southern coast of the Mekong also resemble coastal aquaculture belts (Figure 4b). This could be confirmed via numerous field visits in recent years, as also elucidated in Kuenzer *et al.* [15] as well as Vo *et al*. [66,67].

Inundation at the southwestern tip and coast of the delta is thus driven by human activity, digging and filling up pools to raise shrimp and fish (Figure 5c). For Ca Mau Province (southwestern tip of the delta) the frequently inundated areas (blue tones) coincide for over 80% with aquaculture areas extracted by Vo *et al*., (2013) from SPOT data [67]. The light green, yellowish, and orange areas in the northern part of the Mekong Delta (Figure 4), which are flooded from a few weeks up to half a year, are rice farming areas intensively cultivated to yield two to three harvests annually behind semi-protected to fully protected dykes (Figure 4a,b). This has already been presented in depth by the main author, analyzing a 150 m resolved ENVISAT ASAR WSM time series for the years 2007–2011 [15] as depicted in Figure 5. These authors had already confirmed that irrigation water for this northern area arrives with the river as well as via overland flow with the rainy season starting around June (Figure 5a) [15]. Overall, most of the delta is affected by inundation. Only 40% (15,223 km^2) of the delta area was not inundated on any day of 2013 in the MODIS time series analyzed. About 14% (5443 km^2) of the delta area is inundated up to 30 days, 13% between 31 and 60 days respectively, 8% between 61 and 90 days, 5% between 91 and 120 days, and 5% between 121 and 150 days; all other classes

account for around 2%. The area that is always covered with water (defined as inundation longer than 331 days)—as extracted from this 250 m data set—comprises about 2.5% (957 km^2) of the Mekong Delta area (Figure 4c,d). The results presented for the Mekong Delta coincide well with the inundation patterns derived from higher resolution studies presented in the same journal by Kuenzer *et al.* [15,41]. Features which are never inundated—neither in Figure 4 nor in Figure 5—are elevated hills in the northwest of the delta (see red box), elevated areas with fruit tree orchards in the southern center close to the river's main branches (areas indicated by a green box), and melaleuca forests on the west (yellow box). However, there are also some areas, which—we know—are permanently inundated, but cannot be derived from optical data—such as the water surface below dense mangrove canopy cover in the southwest of the delta right at the "tip".

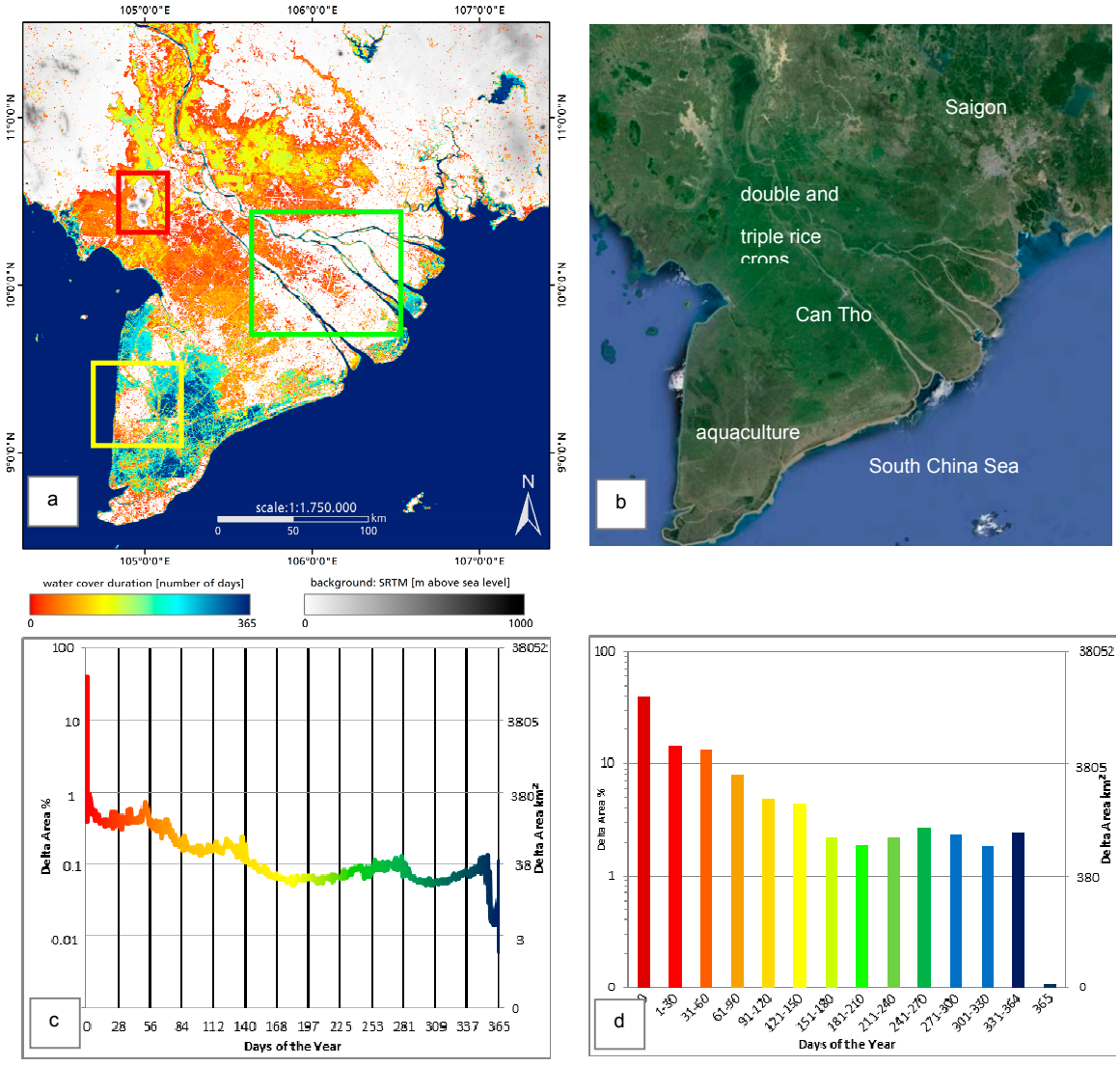

Figure 4. Intra-annual inundation patterns of the Mekong Delta, Vietnam, derived from an annual time series of daily temporal resolution for the year 2013. (**a**) intra-annual inundation dynamics, (**b**) optical data for comparison, (**c**,**d**) quantitative analyses of inundation dynamics

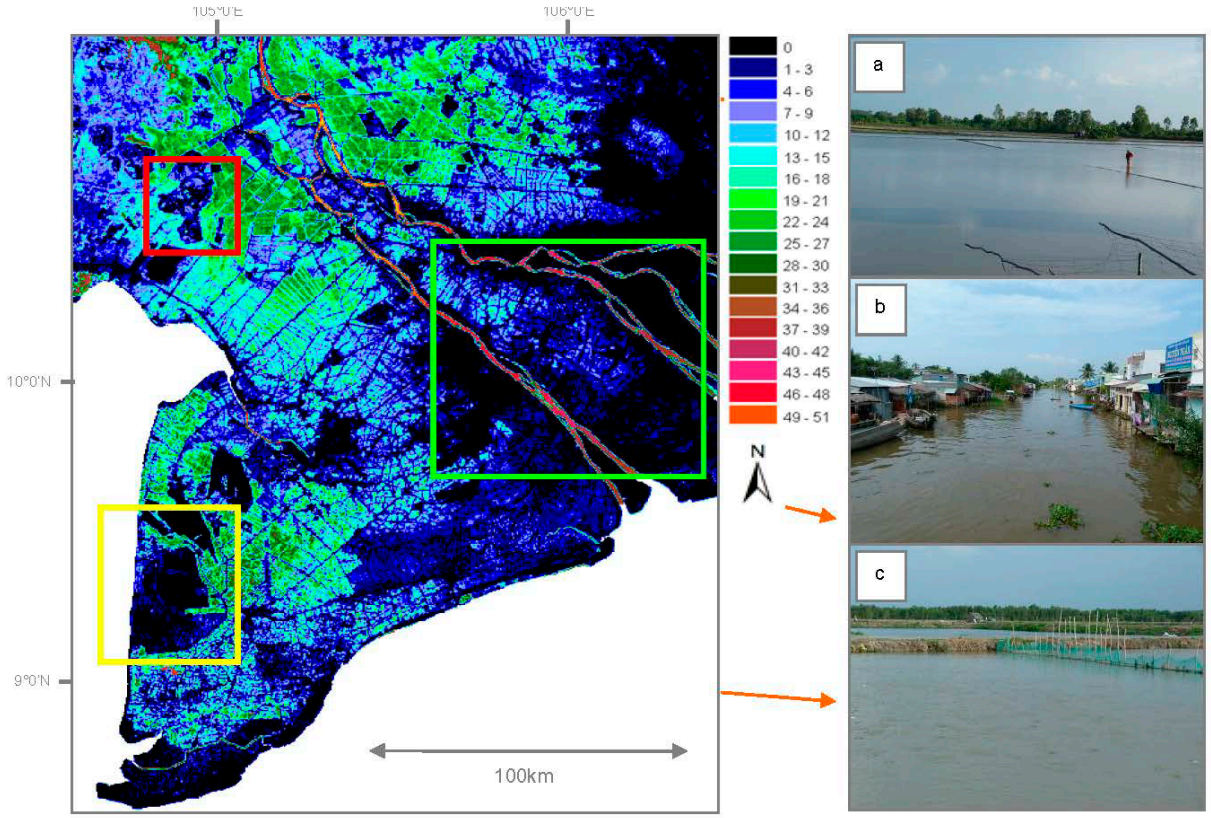

Figure 5. Inundation patterns for the Mekong Delta, as derived from a time series of 150 m resolution ENVISAT ASAR wide swath mode data. An analyses from 51 scenes covering 2007 to 2011 is displayed. Modified based on Kuenzer *et al*. [15]. (**a**) Overland-flow-related natural irrigation water in the northern area of the delta; (**b**) Narrow canals dissecting the delta; (**c**) inundation at the southwestern tip and coast of the delta.

A very similar situation can be revealed for the Irrawaddy Delta in Myanmar. The delta area is framed by small mountain chains to the west and to the northeast of the main river course and its delta branches (Figure 6b). The most prominently inundated areas are the northern floodplains along the western and eastern river branches, as well as the larger region of permanent water coverage close to Rangun (Figure 6a), where aquaculture is rapidly expanding. In the northeastern quarter of Figure 4a the Phy Gyi Reservoir and the Nga Moe Yeik Reservoir can be seen.

The very low lying coastal floodplains in the southeast delta along the Gulf of Martaban were inundated up to 2–3 months per year in 2013. In 2013 70.8% (18,742 km^2) of the delta was not affected by water coverage or inundation according to an analysis based on the 250 m resolution product. However, standing water under vegetation cover will not be extracted by the water detection algorithm. As for all the other deltas – these effects will be addressed in the discussion below.

About 9.8% (2612 km^2) of the delta area is inundated 1–30 days per year, 9% between 31 and 150 days per year, respectively, and about 5% between 151 and 330 days per year. Only 1.3 % (278 km^2) of the delta is covered with water for more than 331 days per year (see Figure 6c,d). Drivers of inundation are—just like for the Mekong Delta—overland flow coming with the monsoonal rainy season based on overland flows from upstream areas, which is used for rice cultivation. Furthermore, in selected areas human control (set up of aquaculture areas) lead to year round water coverage.

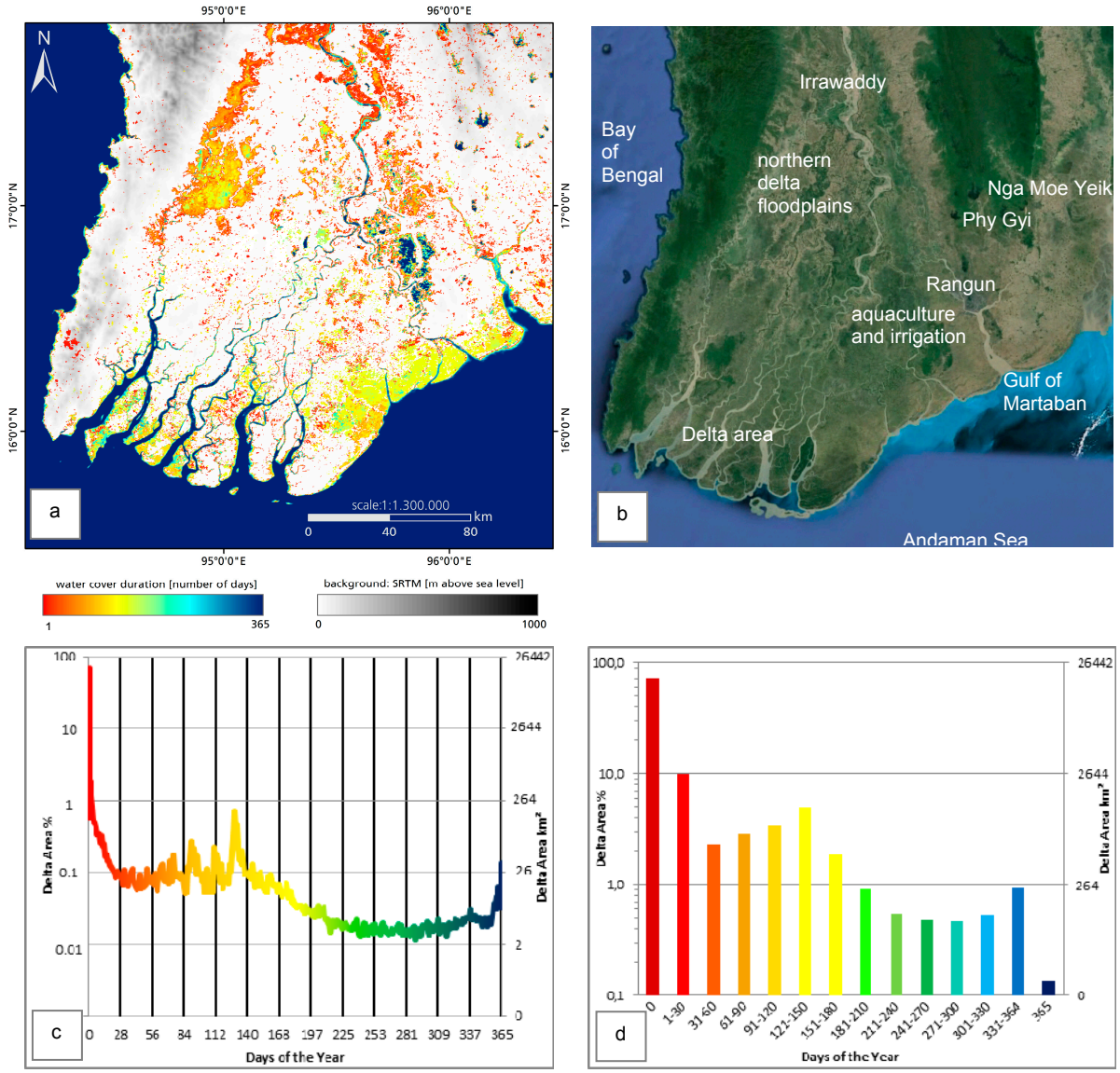

Figure 6. Intra-annual inundation patterns of the Irrawaddy Delta, Myanmar, derived from an annual time series of daily temporal resolution for the year 2013. (**a**) intra-annual inundation dynamics, (**b**) optical data for comparison, (**c**,**d**) quantitative analyses of inundation dynamics

Inundation patterns for the large Ganges Delta area are presented in Figure 7a. The Ganges River, Jamuna River, and Meghna River are clearly extracted as always inundated (dark blue, 365 days). Furthermore, north of the Sundarbans mangrove forest an area of near constant inundation in the western part of the delta stands out. This is a region of intensive aquaculture and irrigation agriculture (see also 7b). Accentuated inundation for about half of the year 2013 can be observed in the northern floodplains of the Bangladesh part of the Ganges Delta. Orange regions indicate areas that are inundated for about one to two months per year. A few outliers can be observed in the very east of Figure 7a—here a few scattered pixels were picked up in a mountainous area, which are most likely shadowed areas and not inundated areas. According to the 250 m resolved intra-annual time series for 2013, 63% (47,187 km^2) of the delta is never inundated; 20% is water covered between 1 and 60 days, and about 12% between two months and 11 months. About 4.3% (3210 km^2) of the area is inundated

for more than 331 days, which can be considered permanent water coverage (Figure 7c,d). However, also in the Ganges Delta areas exist (see green boxes in Figure 7a,b), where we have confirmed water cover on the ground, but where it cannot be seen from space due to dense mangrove canopy above the water surfaces. Water, which is completely covered by vegetation (either dense canopy, or e.g., carpets of water-hyacinths or water lilies covering lakes or river branches *etc.*) are always a problem for any inundation mapping approach. For water coverage under trees future planned L-band microwave data (such as from the envisaged Tandem-L mission) might be one means to detect these below-canopy surfaces at least partially.

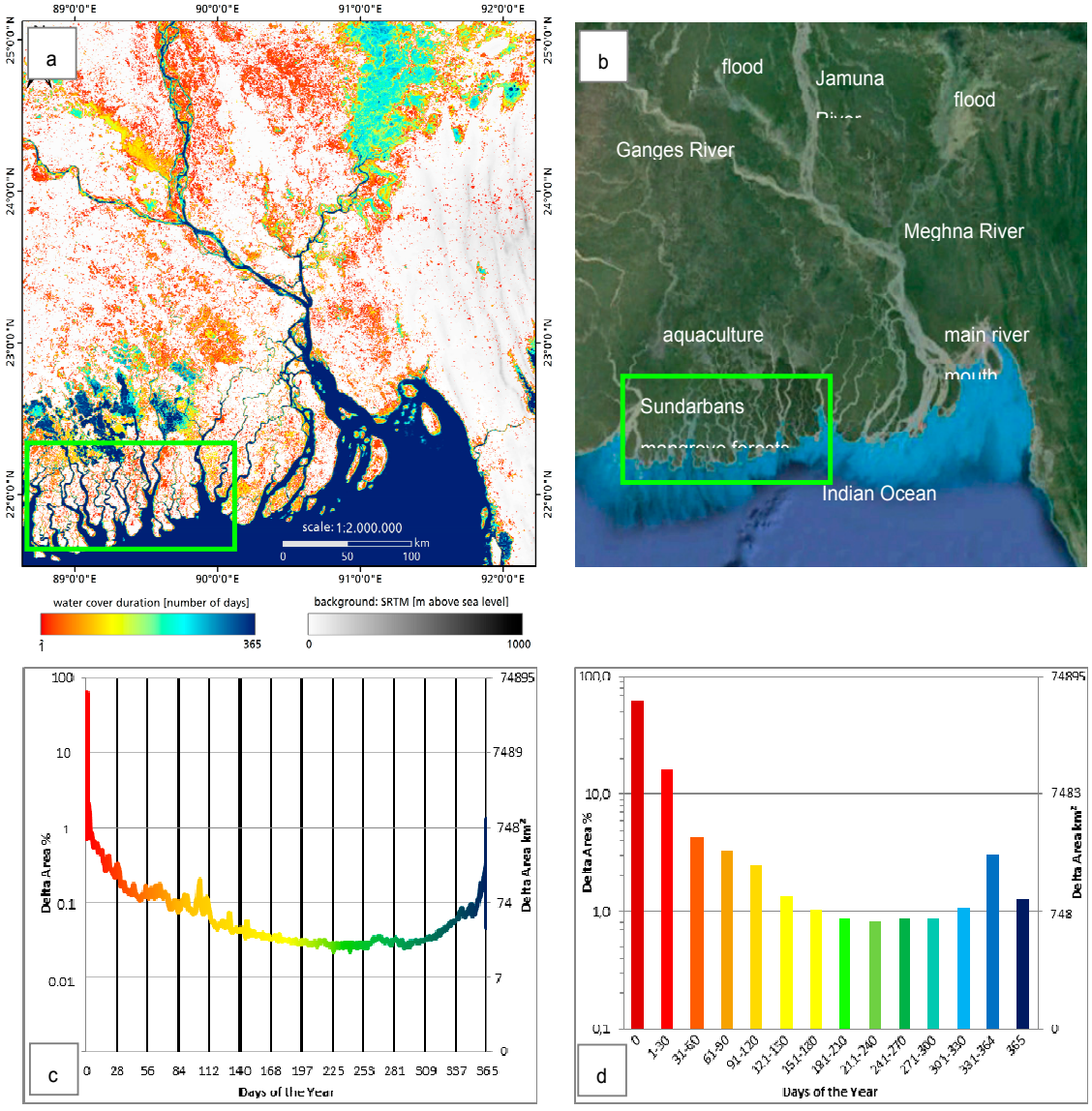

Figure 7. Intra-annual inundation patterns of the Ganges-Brahmaputra Delta in India/Bangladesh, derived from an annual time series of daily temporal resolution for the year 2013. (**a**) intra-annual inundation dynamics, (**b**) optical data for comparison, (**c**,**d**) quantitative analyses of inundation dynamics

The Canadian Mackenzie Delta Region inundation patterns differ from all the Asian river deltas presented above. When interpreting the spatial map of inundation patterns (Figure 8a), the first

noticeable feature is a very distinct difference between the modern delta and the eastern Mackenzie Delta Region uplands. The western part of the region appears in mainly orange and yellowish tones, indicating that nearly all of this area is inundated for at least a few weeks or months per year. These inundation events are presumptively linked to the increasing discharge in late spring, the lifting and break-up of the river ice [68]. Large areas of the delta are then flooded due to the break-up and the rapidly increasing discharge. The ice breaking can happen within a few days if ice jams are ponding the discharge [69]. The eastern part of the Mackenzie Delta Region, by contrast, seems to be inundated less frequently and at shorter intervals. A clear divide, which—at first glance—might be mistakenly interpreted as a data artifact, separates the two parts of the site (Figure 8a).

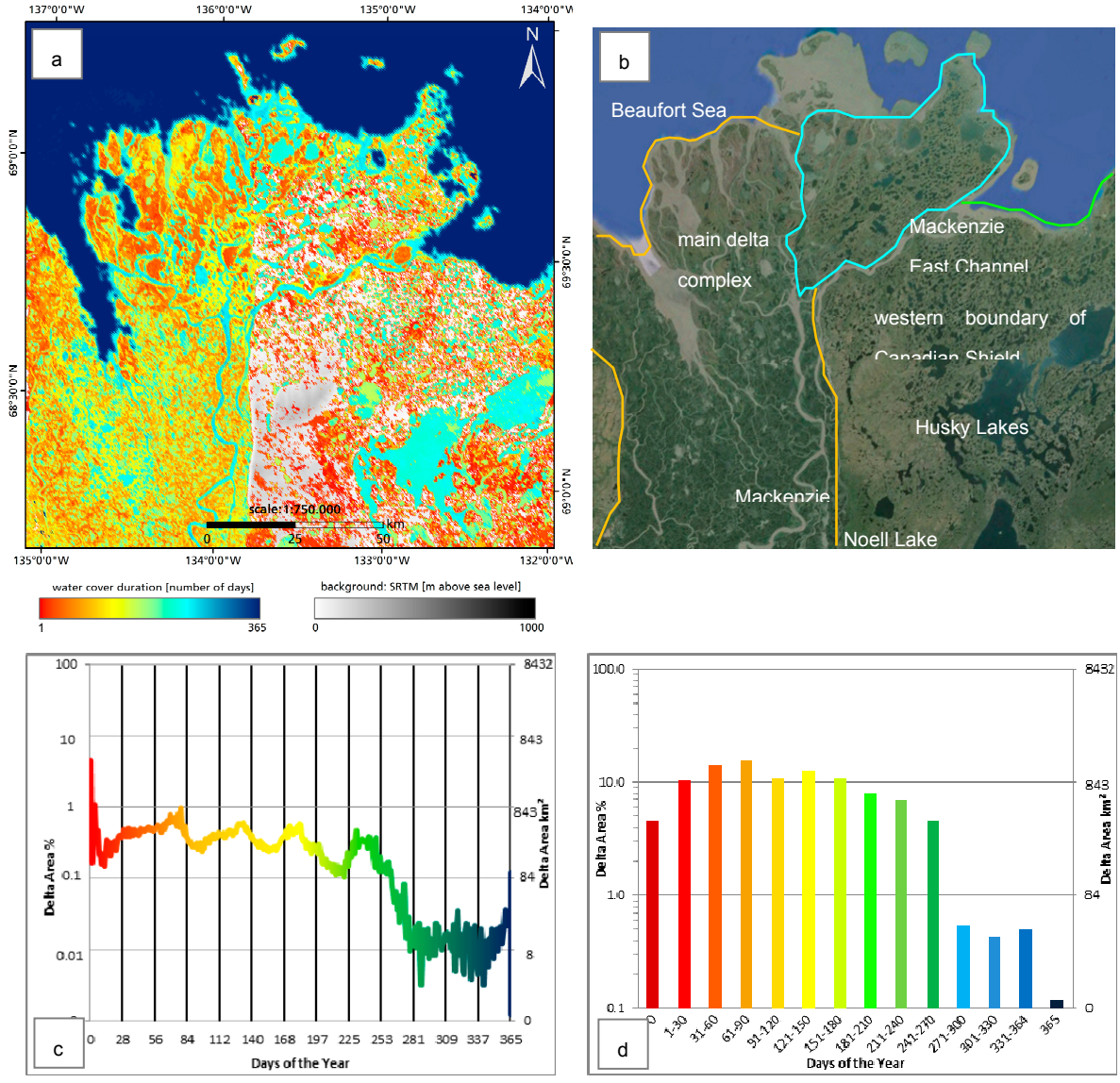

Figure 8. Intra-annual inundation patterns of the Mackenzie Delta Region, Canada, derived from an annual time series of daily temporal resolution for the year 2013. Note that figures c and d represent the main delta complex (within the orange boundary) only. (**a**) intra-annual inundation dynamics, (**b**) optical data for comparison, (**c**,**d**) quantitative analyses of inundation dynamics

The striking contrast between the western and the eastern parts of the area is—however—not an artifact, but reflects the local geology and terrain. While the western half (within the orange marked boundaries) is located at elevations between zero and three meters above sea level, the northeastern part within the turquoise boundary, also named Richards Island, is zero to 35 m above sea level. The southeastern part of the site (east of the green lines) is 10 to 230 m above sea level. A steep cliff of exposed bedrock running north-south characterizes the eastern shore of the Mackenzie River. The modern delta complex of the Mackenzie is bounded to the east by the uplands (e.g., Caribou Hills). This strongly elevated plateau of the eastern delta is the westernmost fringe of the Canadian Shield, however, the surficial geology is dominated by quaternary glacial deposits. Here large lakes, such as the Husky Lakes are embedded. The fact that these as well as other lakes in the delta appear in shades of turquoise to light green and not in dark blue (dark blue indicating water cover 365 days per year) is because the lakes are frozen for much of the fall, winter, and early spring (Figure 6a). The same applies to the Mackenzie River itself and its branches, which are also depicted in turquoise. As precipitation in the area is low, all water bodies and inundation mainly originate from the river's influences, snowmelt events, as well as thawing permafrost [46].

Overall, only 4.5% (385 km^2) of the delta area analyzed and presented in Figure 6a as never inundated or water covered. About 95.4% (8009 km^2) is more or less frequently water covered. As the Mackenzie Delta Region is an arctic environment, inundation duration has to be interpreted with care, as frozen periods and snow-cover periods impact inundation. Overall, inundation for more than 210 days is rare. Some 45% of the delta is inundated up to three months, and a further 25% up to half of the year. Areas which are water covered for more than 180 days per year sum up to around 22% (1854 km^2) of the respective area.

Table 2 depicts all delta areas, as well as the percentages and km^2 of inundation in the individual classes for varying inundation length. Furthermore, the drivers of inundation are elucidated. Whereas all Asian river deltas depict very similar inundation characteristics (compare Figures 2c to 5c) the inundation characteristics of the only polar delta are clearly influences by freeze-thaw processes and show a much stronger variability within the individual inundation length classes. In this region areas that are inundated year round do basically not exist—which can be explained with the fact that most of the area is frozen/snow covered for more than one third of the year. Table 1 below summarizes the inundation patterns for the five selected river deltas.

Figure 9 depicts one possible validation approach. Next to the indirect comparisons with SAR-derived inundation information (as qualitatively undertaken for the Mekong, but not comparing the same year), or based on the comparison with land use information (as undertaken for the Yellow River Delta for the same year) as presented in Figures 3 and 5, it is also possible to compare the MODIS derived "water masks" with "water masks" extracted from higher resolution optical data, such as Landsat. We therefore had to find Landsat data available for the same area on exactly the same day and compare it with the MODIS derived product. Figure 9 depicts this approach for part of the Ganges Delta evaluated on DOY 310 in 2013 (left), and for part of the south-eastern Mackenzie Delta Region (right), validated on DOY 214. The white frame in Figure 9a,b indicates the frame of the Landsat scene. To perform an accuracy assessment, water surfaces were extracted from the Landsat scenes based on a supervised image classification approach. In this way, "water masks" of MODIS and such derived of Landsat were available. The MODIS derived water masks were the resampled to the same

resolution of Landsat so that it was possible to assess commonalities and discrepancies. As indicated in the legend of Figure 9a,b dark blue areas are regions where the MODIS derived product and the Landsat derived product coincide for 100%. The lighter the blue-ish tone, the less agreement. Light blue areas indicate regions where water cover has still been detected in the coarse resolution MODIS pixel, but in Landsat data it can be seen that actually only about 50% of that MODIS pixel are water covered (see also Figure 9c, upper case). In greenish tones we displayed areas, which have not been detected as water covered in the MODIS derived product, but show a bit of water coverage in the Landsat data. The mixed-pixel effect here becomes obvious: MODIS pixels in which water cover exceeds a certain percentage are detected as inundated (the overall spectral reflectance in the NIR is low enough), whereas in some coarse resolution pixels water surfaces are so few that the overall pixel's reflectance is not lowered enough to be picked up as water.

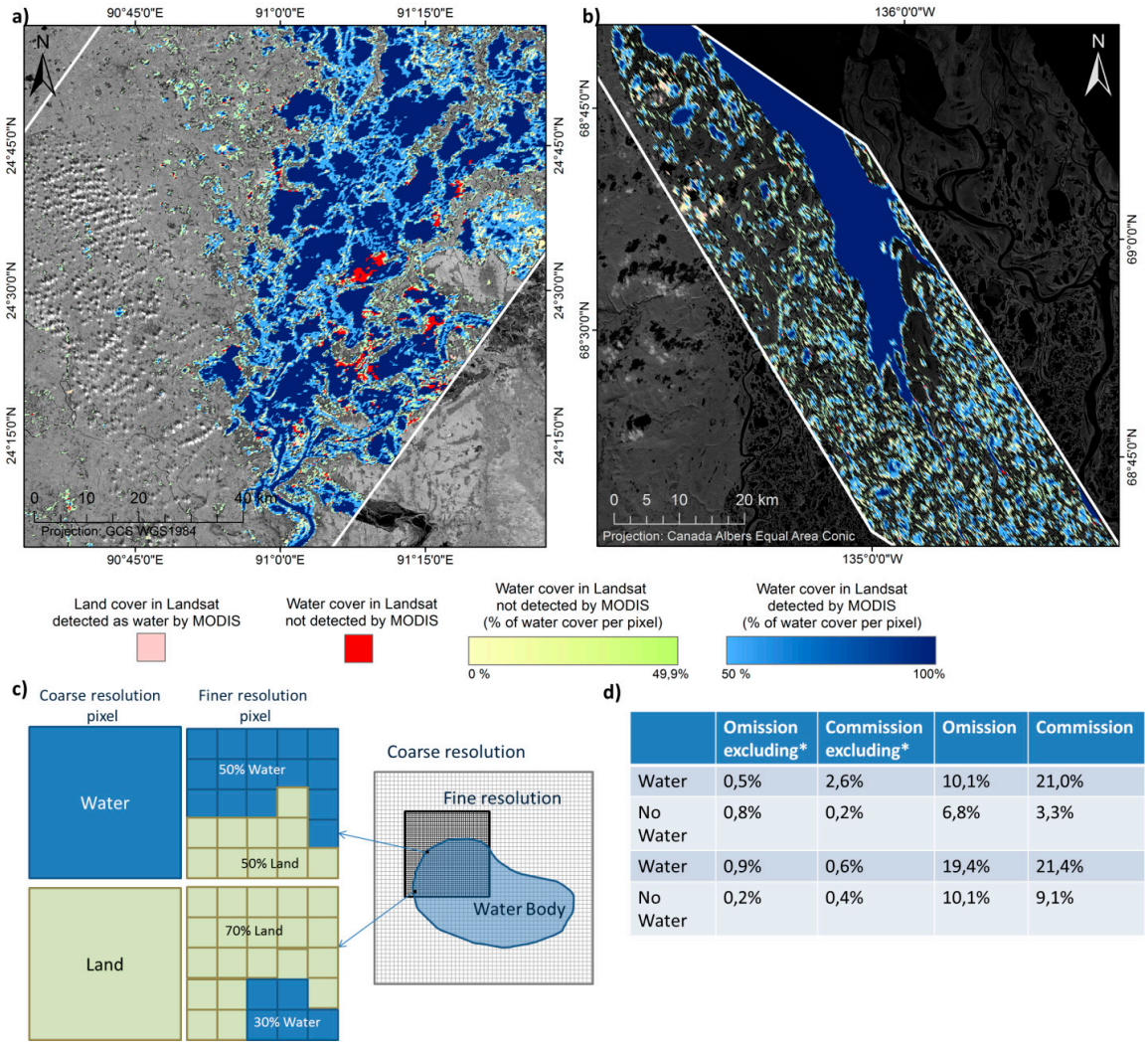

	Omission excluding*	Commission excluding*	Omission	Commission
Water	0,5%	2,6%	10,1%	21,0%
No Water	0,8%	0,2%	6,8%	3,3%
Water	0,9%	0,6%	19,4%	21,4%
No Water	0,2%	0,4%	10,1%	9,1%

Figure 9. Validating the MODIS derived daily inundation ("water mask") with water surfaces derived from higher resolution Landsat data of the same day. (**a**,**b**) representation of water coverage derived from MODIS and Landsat data respectively, (**c**) schmetic sketch of the mixed pixel phenomenon, (**d**) omission and commission errors.

Table 2. Inundation patterns of the year 2013, for the five selected river deltas.

	Yellow River Delta	**Mekong Delta**	**Irrawaddy Delta**	**Ganges Delta**	**Mackenzie Delta**
Overall area	3732.16 km^2 (100%)	38052.22 km^2 (100%)	26443.31 km^2 (100%)	74897.79 km^2 (100%)	8431.36 km^2 (100%)
Never inundated	1813.22 km^2 (48.58%)	15223.97 km^2 (40.01%)	18742.39 km^2 (70.88%)	47187.34 km^2 (63.00%)	385.53 km^2 (4.57%)
1–30 times	556.34 km^2 (14.90%)	5443.21 km^2 (14.30%)	2612.13 km^2 (9.88%)	11977.9 km^2 (15.99%)	880.05 km^2 (10.44%)
31–60 days	181.81 km^2 (4.87%)	5079.20 km^2 (13.35%)	615.10 km^2 (2.33%)	3165.73 km^2 (4.23%)	1193.02 km^2 (14.15%)
61–90 days	116.88 km^2 (3.13%)	2990.62 km^2 (7.86%)	757.10 km^2 (2.86%)	2490.95 km^2 (3.33%)	1331.37 km^2 (15.79%)
91–120 days s	80.49 km^2 (2.16%)	1849.23 km^2 (4.86%)	885.04 km^2 (3.35%)	1899.83 km^2 (2.54%)	912.03 km^2 (10.82%)
121–150 days	63.10 km^2 (1.69%)	1689.58 km^2 (4.44%)	1299.70 km^2 (4.92%)	1020.32 km^2 (1.36%)	1069.27 km^2 (12.68%)
151–180 days	74.86 km^2 (2.01%)	816.67 km^2 (2.15%)	496.67 km^2 (1.88%)	775.83 km^2 (1.04%)	907.25 km^2 (10.76%)
181–210 days	67.89 km^2 (1.82%)	717.17 km^2 (1.88%)	238.27 km^2 (0.90%)	655.78 km^2 (0.88%)	676.39 km^2 (8.02%)
211–240 days	81.19 km^2 (2.18%)	815.33 km^2 (2.14%)	144.14 km^2 (0.55%)	605.01 km^2 (0.81%)	587.31 km^2 (6.97%)
241–270 days	101.64 km^2 (2.72%)	1017.00 km^2 (2.67%)	127.88 km^2 (0.48%)	647.14 km^2 (0.86%)	388.16 km^2 (4.60%)
271–300 days	146.45 km^2 (3.92%)	879.30 km^2 (2.31%)	124.66 km^2 (0.47%)	647.89 km^2 (0.87%)	45.67 km^2 (0.54%)
301–330 days	154.07 km^2 (4.13%)	692.22 km^2 (1.82%)	139.85 km^2 (0.53%)	804.48 km^2 (1.07%)	36.38 km^2 (0.43%)
331–364 days	215.41 km^2 (5.77%)	916.32 km^2 (2.41%)	243.10 km^2 (0.92%)	2278.3 km^2 (3.04%)	41.97 km^2 (0.50%)
Constantly inundated	93.86 km^2 (2.51%)	41.16 km^2 (0.11%)	35.37 km^2 (0.13%)	932.36 km^2 (1.24%)	10.14 km^2 (0.12%)
Drivers of inundation	Aquaculture, water storage, irrigation agriculture, wetlands	Irrigation agriculture, aquaculture, river and overland flooding	River floodplains, irrigation agriculture, limited aquaculture	Irrigation agri- and aquaculture, wetlands, inlets and pools	Thermokarst lakes and pools, snowmelt, wetland swamps

Special cases are red areas which are regions that were water covered in the Landsat product, however, as can be seen in Figure 9a,b the MODIS derived and the Landsat derived water products coincide very well, and discrepancies only occur as had to be expected – in the boundary regions of the water bodies due to the mixed pixel effects. The small Table d in Figure 9, as well as Tables 3 and 4 below, quantitatively elucidate the error of omission and the error of commission derived from the comparison of the products. In Figure 9d the left two columns indicate these errors excluding areas with a Landsat-derived water fraction of less than 50%, whereas the right two columns only consider the bluish (above 50%, upper case in Figure 9c) areas. The validation indicates a products accuracy ranging between 79% and 99%, this goes in line with similar product validations presented by Klein *et al*. [27].

Table 3. Accuracy tables for the Ganges Delta, year 2013, day of the year 310.

Error Matrix Excluding Transition Zone (Landsat Water Fraction > 50%)					
Landsat/MODIS	**Water**	**No Water**	**Total**	**Omission**	**Commission**
Water	540,420	2660	543,080	0.5%	2.6%
No Water	14,190	1,732,430	1,746,620	0.8%	0.2%
Total	554,610	1,735,090	2,272,850		
Error Matrix taking the transition zone into account (Landsat fraction < 50%)					
Landsat/MODIS	**Water**	**No Water**	**Total**	**Omission**	**Commission**
Water	540,420	60,460	600,580	10.1%	21.0%
No Water	126,150	1,732,430	1,858,580	6.8%	3.3%
Total	666,570	1,792,890	2,272,850		

Table 4. Accuracy tables for the Mackenzie Delta Region, year 2013, day of the year 214.

Error Matrix Excluding Transition Zone (Landsat Water Fraction > 50%)					
Landsat/MODIS	**Water**	**No Water**	**Total**	**Omission**	**Commission**
Water	171,400	1560	172,960	0.9%	0.6%
No Water	960	407,540	408,500	0.2%	0.4%
Total	172,360	409,100	578,940		
Error Matrix taking the transition zone into account (Landsat fraction < 50%)					
Landsat/MODIS	**Water**	**No Water**	**Total**	**Omission**	**Commission**
Water	171,400	41,240	212,640	19.4%	21.4%
No Water	45,520	407,540	453,060	10.1%	9.1%
Total	216,920	448,780	578,940		

5. Discussion

As with any coarse resolution product, a water product derived from daily MODIS reflectance data brings with it the advantage of extremely high temporal resolution as well as the weakness of relatively low spatial resolution at 250 m. Whereas the high temporal resolution allows discovery of intra-annual inundation patterns, the 250 m spatial resolution increases the probability of mixed pixels. Therefore, quantitative analyses of inundation coverage in the individual deltas have to be handled with care. Small water covered areas in a 250 m pixel might not influence the overall spectral

signature of a pixel strongly enough to lead to an overall decrease in NIR reflectance. Water bodies much smaller than a MODIS pixel will definitely be missed. This is evident for the Mekong Delta, for example, where the area constantly covered with water is (in reality) actually quite large, as the delta is dissected by a complex network of canals and other waterways. However, these canals are too small in width to be identified in 250 m MODIS data. Furthermore, water bodies and inundation under vegetation (e.g., below a dense mangrove canopy or a closed mat of water lilies) cannot be detected [70]. Also, water, which is too sediment-laden (as could be seen in the Yellow River Delta) might not always be detected as water [71]. Wang *et al.* (2005) have elucidated the large impact of the water-sediment regulation scheme (WSRS) for the Yellow River on the sediment supply of the river in the river mouth area [71]. This all leads to an underestimation of water covered surfaces. At the same time, some pixels which are identified as inundated might only be partially water-covered. This, as well as erroneous signals from shadows in steep terrain (an effect which is, however, very rare in flat river deltas) can also lead to an overestimation of water surfaces. Overall, the inundation patterns and intra-annual inundation curves presented for the five river deltas coincide well with our indirect and direct validation approaches, as well as with other studies undertaken by the authors, which analyzed inundation information for areas in the deltas based on higher resolution optical or SAR data. Furthermore, they match the features discernible with highest resolution optical imagery, such as that available in Google Earth or Landsat derived land use maps. Direct and multi-temporal quantitative validation of the products for areas of such enormous extent is impossible, as is the case for most remote sensing derived global information products. However, direct and indirect validation was carried out based on higher resolution Landsat data, and the overall accuracy of the methodology presented yields water body mapping accuracies of between 79% and 99%.

Additionally, it should be mentioned that the detection accuracy of the method employed for water surface extraction could be improved if further MODIS bands were included in the processing chain. For example, the integration of a thermal band could facilitate the difficult distinction between water bodies and cloud shadow, assuming that—despite the shadowing effect—water bodies exhibit different temperature characteristics than—even shadowed—land surfaces. However, the analyses presented here are based on data of 250 m spatial resolution. The MODIS thermal bands have a resolution of 1 km, and their integration would therefore drastically decrease the spatial resolution of the product and the level of detail in inundation patterns that can be derived. The same applies to bands in the mid-infrared, which have a 500 m spatial resolution. Thus, one approach, which could be applied to slightly improve the products' accuracy without lowering the spatial resolution and without drastically increasing data processing time could be the integration of the red band (NDVI approach). In the future, the approach will furthermore benefit from novel static water mask products and a high resolution DEM based on the TanDEM-X Mission as well as water body products derived from novel Sentinel-1 data, which are currently under development by different groups. These could improve the methodic step of training data generation at higher accuracy.

Additionally, we envisage to improve the mapping approach with respect to threshold stability used for water surface extraction. Actually, the reflectance threshold determined on a daily basis derived from averaged training data pixels defined by permanent water body products is relatively stable over the course of a year, although variation occurs due to varying factors such as varying surface roughness, sudden changes on chlorophyll content or turbidity *etc*. This is a phenomenon we need to

investigate at greater depth. It can be assumed that in most regions of the world thresholds are characterized by a "seasonal" behavior depending on seasonal water constituent variation.

Furthermore, it should be mentioned that we aim to extend the time series approach presented here to all river deltas areas globally, as well as to all available years of MODIS coverage. As we are interested in trends during this 15 year time span (e.g., shifts in inundation start and end *etc.*) we purposely did not work with eight day composite products, but with daily data. However, great examples using up to 526 MODIS eight day composites have been presented by Ogilvie *et al.* [72], monitoring flood dynamics in Niger Inner Delta (an inland delta). These authors had hydro-meteorological data available to correlated flood area extent extracted from the satellite data with the flood stage. Similar studies comparing MODIS derived flood information and hydrological data were presented by Crétaux *et al.* [73]. Also Leauthaud *et al*. [74] had such data available to related flood extents to water levels and meteorological data. We therefore envisage to collect such data for our main river delta areas of interest as well, to perform similar studies, as presented by these authors.

6. Conclusions and Outlook

Whereas SAR data of higher spatial resolution is and will remain the preferred choice for most studies focusing on flood and inundation detection at high accuracy [15,16], coarse spatial resolution but temporally dense time series of inundation information derived from optical sensors allow for the revelation of intra-annual dynamics and overall inundation patterns for very large areas. Based on daily, freely available Moderate Resolution Imaging Spectrometer, MODIS, data of the year 2013 we generated an intra-annual time series at 250m spatial resolution, covering the large river delta areas of the Yellow River Delta in China, the Mekong Delta in Vietnam, the Irrawaddy Delta in Myanmar, the Ganges-Brahmaputra Delta in India/Bangladesh, as well as the polar Mackenzie Delta in northwestern Canada. Based on 4380 MODIS scenes (six tiles covering the five deltas, each tile acquired two times per day, for 365 days) of the red band of the MOD09GQ and MYD09GQ reflectance product (platforms Terra and Aqua) water surfaces were derived for each day of the year. This was undertaken based on automatic training data and threshold generation supported by the MOD44W static water mask and including information on cloud, and snow cover extracted from the MOD10A1 and MYD10A1 products. The resulting daily water/non-water products for the six river deltas allowed for the generation of an overall inundation length product, depicting for each pixel how often it is water covered over the course of one year. Inundation patterns for the five river deltas were quantitatively analyzed, and phenomena observed were explained with support of *in-situ* knowledge and high resolution optical data. Overall, clear differences can be observed between the four densely inhabited Asian river deltas located in the mid latitude and subtropical zone, *versus* the polar Mackenzie Delta. Large proportions of the Asian river deltas are never affected by inundation (48%, 405, 70%, 63% for the Yellow-, Mekong-, Irrawaddy-, and Ganges Delta respectively). Inundation patterns in the four Asian deltas are largely impacted by irrigation agriculture, aquaculture, as well as some river and overland related flooding. The Yellow River Delta results depicting inundation dynamics (Figure 2) have been compared with a detailed land use classification derived from Landsat data for the same year. The frequently inundated (dark blue) areas along the coast derived from the intra-annual MODIS time series clearly coincide with the aquaculture areas in the land use product at higher resolution

(which is under preparation for publication). Furthermore, the first author has been in the Yellow River Delta repeatedly, and thus inundation patterns could be validated based on in-depth field knowledge and
GPS photographs.

In the polar, nearly uninhabited Mackenzie Delta, which is influenced by thermokarst and snow melt processes, and which contains over 48.000 little lakes during the summer period, only 4.6% of the delta is never affected by inundation. Intra-annual inundation curves presented for the four deltas indicate similar inundation length patterns of low variability for the four mid-latitude / subtropical deltas, whereas areas of differing inundation length show a greater variability for the polar delta. Therefore, results presented indicate that inundation occurs in the analyzed river delta sites at defined spatio-temporal patterns. These patterns can be linked to the individual site's hydrological and geomorphologic specifics as well as human impact in the area. However, existing field and expert knowledge of the areas was necessary to interpret results and avoid misinterpretation and misleading conclusions. The coarse spatial resolution of results goes along with increased probability of mixed pixel phenomena and an underestimation of the inundation surface, as small water bodies cannot be detected. However, the high temporal resolution allowed for pattern derivation at a spatial extent (large areas) and temporal density that can hardly be achieved with any other type of data.

The approach presented here is currently being extended to additional river deltas, covering not only one year but all years with available MODIS data. In the long term it will be of interest to analyze spatial as well as inter-annual patterns of inundation and water body coverage for river deltas on all continents and in all climate zones. This will support the categorization of these ecosystems and reveal overall similarities or differences that can be attributed to different drivers. Challenges would be the large amount of required data processing as well as the direct or indirect validation of products. Within the next few years the approach presented can furthermore be adapted to higher resolution data, such as from the Landsat and Sentinel-2 sensor, although a loss of temporal resolution would then accompany the improved spatial resolution. As river deltas are one of the most densely settled, most dynamic, and most threatened ecosystems on earth, any remote sensing based time series analyses that improves our general understanding of these areas are urgently needed.

Acknowledgments

Special thanks go to NASA, NOAA, USGS, and NSIDC for providing the data and download services for the data used in this study. The authors furthermore thank L. Lambrecht for support with charts. The work presented was undertaken in the context of the Belmont Forum project Sustainable DELTAS.

Author Contributions

Claudia Kuenzer led the research design and data processing, quantitatively analyzed the inundation dynamics and has authored the manuscript. Igor Klein undertook most of the MODIS data processing and generated several figures. Tobias Ullmann contributed his expertise on the Mackenzie River Delta Region and authored the introductory section on the Mackenzie Region. Efi Foufoula Georgiou supported data processing through constructive criticism, contributed general knowledge on delta

inundation dynamics, and worked over the final version of the manuscript. Roland Baumhauer and Stefan Dech commented on the manuscript and thus helped to substantially improve its quality.

Conflicts of Interest

The authors declare no conflict of interest.

References

1. Martinis, S.; Twele, A.; Kersten, J. A fully automated TerraSAR-X based flood service. *ISPRS J. Photogramm*. **2014**, doi:10.1016/j.isprsjprs.2014.07.014.
2. Jawak, S.D.; Luis, A.J. A rapid extraction of water body features from antarctic coastal oasis using very high-resolution satellite remote sensing data. *Aquati. Procedia* **2015**, *4*, 125–132.
3. Greifeneder, F.; Wagner, W.; Sabel, D.; Naeimi, V. Suitability of SAR imagery for automatic flood mapping in the Lower Mekong basin. *Int. J. Remote Sens.* **2014**, *35*, 2857–2874.
4. Henry, J.-B.; Chastanet, P.; Fellah, K.; Desnos, Y.-L. Envisat multi-polarized ASAR data for flood mapping. *Int. J. Remote Sens.* **2006**, *27*, 1921–1929.
5. Hoque, R.; Nakayama, D.; Matsuyama, H.; Matsumoto, J. Flood monitoring, mapping and assessing capabilities using RADARSAT remote sensing, GIS and ground data for Bangladesh. *Nat. Hazards* **2010**, *58*, 525–548.
6. Gstaiger, V.; Gebhardt, S.; Huth, J.; Wehrmann, T.; Kuenzer, C. Multi-sensoral and automated derivation of inundated areas using TerraSAR-X and ENVISAT ASAR data. *Int. J. Remote Sens*. **2012**, *33*, 7291–7304.
7. Hess, L.L.; Melack, J.M.; Filoso, S.; Wang, Y. Delineation of inundated area and vegetation along the amazon floodplain with the SIR-C synthetic aperture radar. *IEEE Trans. Geosci. Remote Sens.* **1995**, *33*, 896–904.
8. Hess, L.L.; Melack, J.M.; Novo, E.M.L.M.; Barbosa, C.C.F.; Gastil, M. Dual-season mapping of wetland inundation and vegetation for the central Amazon basin. *Remote Sens. Environ.* **2003**, *87*, 404–428.
9. Kuenzer, C.; Knauer, K. Remote sensing of rice crop areas—A review. *Int. J. Remote Sens*. **2013**, *34*, 2101–2139.
10. Mason, D.C.; Speck, R.; Devereux, B. Flood detection in urban areas using TerraSAR-X. *IEEE Trans. Geosci. Remote Sens.* **2010**, *48*, 882–893.
11. Kiage, L.M.; Walker, N.D.; Balasubramanian, S.; Babin, A.; Barras, J. Applications of Radarsat-1 synthetic aperture radar imagery to assess hurricane-related flooding of coastal Louisiana. *Int. J. Remote Sens.* **2005**, *26*, 5359–5380.
12. Lang, M.W.; Kasischke, E.S.; Prince, S.D.; Pittman, K.W. Assessment of C-band synthetic aperture radar data for mapping and monitoring Coastal Plain forested wetlands in the Mid-Atlantic Region, U.S.A. *Remote Sens. Environ*. **2008**, *112*, 4120–4130.
13. Kasischke, E.S.; Smith, K.B.; Bourgeau-Chavez, L.L.; Romanowicz, E.A.; Brunzell, S.; Richardson, C.J. Effects of seasonal hydrologic patterns in south Florida wetlands on radar backscatter measured from ERS-2 SAR imagery. *Remote Sens. Environ.* **2003**, *88*, 423–441.

14. Kuenzer, C.; Huth, J.; Martinis, S.; Lu, L.; Dech, S. SAR time series for the analysis of inundation patterns in the Yellow River Delta, China. In *Remote Sensing Time Series: Revealing Land Surface Dynamics*; Kuenzer, C., Dech, S., Wagner, W., Eds.; Springer Netherland: Dordrecht, The Netherlands, 2015.
15. Kuenzer, C.; Guo, H.; Leinenkugel, P.; Huth, J.; Li, X.; DECH, S. Flood mapping and flood dynamics of the Mekong Delta: An ENVISAT-ASAR-WSM based time series analyses. *Remote Sens.* **2013**, *5*, doi:10.3390/rs5020687.
16. Kuenzer, C.; Guo, H.; Schlegel, I.; Vo, Q.T.; Li, X.; DECH, S. Scale and the capability of Envisat ASAR-WSM, TerraSAR-X Scansar, and TerraSAR-X Stripmap data to assess urban flood situations: A case study in Can Tho Province of the Mekong Delta. *Remote Sens.* **2013**, *5*, 5122–5142.
17. Ulaby, F.T.; Long. D.G. *Microwave Radar and Radiometric Remote Sensing*; University of Michigan Press: Ann Arbor, MI, USA, 2014.
18. Werle, D.; Martin, T.C.; Hasan, K. Flood and coastal zone monitoring in Bangladesh with Radarsat ScanSAR: Technical experience and institutional challenges. *J. Hopkins APL Tech. D* **2001**, *21*, 148–154.
19. Matgen, P.; Hostache, R.; Schumann, G.; Pfister, L.; Hoffman, L.; Svanije, H.H.G. Towards and automated SAR based flood monitoring system: Lessons learned from two case studies. *Phys. Chem. Earth* **2011**, *36*, 241–252.
20. Pierdicca, N.; Pulvirenty, L.; Chini, M.; Guerriero, L.; Candela, L. Observing floods from space: Experience gained from COSMO-SkyMed observations. *Acta Astronautica* **2013**, *80*, 122–133.
21. Martinis, S.; Twele, A. A hierarchical spatio-temporal Markov model for improved flood mapping using multi-temporal X-band SAR data. *Remote Sens*. **2010**, *2*, 2240–2258.
22. Martinis, S.; Twele, A.; Voigt, S. Unsupervised extraction of flood-induced backscatter changes in SAR data using Markov image modeling on irregular graphs. *IEEE Trans. Geosci. Remote Sens.* **2011**, *49*, 251–263.
23. Martinis, S.; Twele, A.; Voigt, S. Towards operational near-real time flood detection using a split-based automatic thresholding procedure on high resolution TerraSAR-X data. *Nat. Hazard. Earth Sys.* **2009**, *9*, 303–314.
24. Kuenzer, C.; Ottinger, M.; Liu, G.; Sun, B.; Dech, S. Earth observation-based coastal zone monitoring of the Yellow River Delta: Dynamics in China's second largest oil producing region over four decades. *Appl. Geogr.* **2014**, *55*, 92–107.
25. Zhou, C.; Luo, J.; Yang, C.; Li, B.; Wang, S. Flood monitoring using multi-temporal AVHRR and Radarsat imagery. *Photogramm. Eng. Remote Sens.* **2000**, *66*, 633–638.
26. Chaouch, N.; Temimi, M.; Hagen, S.; Weishampel, J.; Medeiros, S.; Khanbilvardi, R. A synergetic use of satellite imagery from SAR and optical sensors to improve coastal flood mapping in the Gulf of Mexico. *Hydrol. Process.* **2011**, *26*, 1617–1628.
27. Klein, I.; Dietz, A.J.; Gessner, U.; Galayeva, A.; Myrzakhmetova, A.; Kuenzer, C. Evaluation of seasonal water body extents in Central Asia over the past 27 years derived from medium-resolution remote sensing data. *Int. J. Appl. Earth Obs.* **2014**, *26*, 335–349.
28. Auynirundronkool, K.; Chen, N.; Peng, C.; Yang, C.; Gong, J.; Silapathong, C. Flood detection and mapping of the Thailand Central plain using Radarsat and MODIS under a sensor web environment. *Int. J. Appl. Earth Obs.* **2012**, *14*, 245–255.

29. Sakamoto, T.; Nguyen, N.V.; Kotera, A.; Ohno, H.; Ishitsuka, N.; Yokozawa, M. Detecting temporal changes in the extent of annual flooding within the Cambodia and the Vietnamese Mekong Delta from MODIS time-series imagery. *Remote Sens. Environ.* **2007**, *109*, 295–313.
30. Dietz, A.; Kuenzer, C.; CONRAD, C. Snow cover variability in Central Asia between 2000 and 2011 derived from improved MODIS daily snow cover products. *Int. J. Remote Sens.* **2013**, *34*, 3879–3902.
31. Kuenzer, C.; Renaud, F. Climate change and environmental change in river Deltas Globally. In *The Mekong Delta System—Interdisciplinary Analyses of a River Delta*; Renaud, F., Kuenzer, C., Eds.; Springer Netherland: Dordrecht, The Netherlands, 2012; pp. 7–48.
32. Kuenzer, C.; van Beijma, S.; Gessner, U.; Dech, S. Land surface dynamics and environmental challenges of the Niger Delta, Africa: Earth observation based analyses spanning three decades (1986–2013). *Appl. Geogr.* **2014**, *53*, 354–368.
33. Ericsson, J.P.; Vörösmarty, C.J.; Dingman, S.L.; Ward, L.G.; Meybeck, M. Effective sea-level rise and deltas: Causes of change and human dimension implications. *Glob. Planet. Chang.* **2006**, *50*, 63–82.
34. Renaud, F.; Syyvistski, J.P.M.; Sebesvari, S.; Werners, S.; Kremer, H.; Kuenzer, C.; Jeuken, A.; Ramachandran, R.; Friedrich, J. Tipping from the Holocene to the Anthropocene: How threatened are major world deltas? *Curr. Opin. Environ. Sustain*. **2014**, *5*, 644–654.
35. Ye, Q.; Liu, G.; Tian, G.; Chen, S.; Huang, C.; Chen, S.; Liu, Q.; Chang, J.; Shi, Y. Geospatial-temporal analysis of land-use changes in the Yellow River Delta during the last 40 years. *Earth Sci.* **2004**, *47*, 1008–1024.
36. Zhang, T.T.; Zhao, B. Impact of anthropogenic land-uses on salinization in the Yellow River Delta, China: Using RS-GIS statistical model. *Int. Arch. Photogramm. Remote Sens. Spat. Inf. Sci.* **2010**, *38*, 545–561.
37. Higgins, S.; Overeem, I.; Tanaka, A.; Syvistski, J. Land subsidence at aquaculture facilities in the Yellow River delta, China. *Geophys. Res. Lett.* **2013**, *40*, 3898–3902.
38. Bi, X.; Wang, B.; Lu, Q. Fragmentation effects of oil wells and roads on the Yellow River Delta, North China. *Ocean Coast. Manag.* **2011**, *54*, 256–264.
39. Ottinger, M.; Kuenzer, C.; Liu, G.; Wang, S.; Dech, S. Monitoring land cover dynamics in the Yellow River Delta from 1995 to 2010 based on Landsat 5 TM. *Appl. Geogr.* **2013**, *44*, 53–68.
40. Renaud, F.; Kuenzer, C. The water-development nexus: Importance of knowledge, information and cooperation in the Mekong Delta. In *The Mekong Delta System—Interdisciplinary Analyses of A River Delta*; Renaud, F., Kuenzer, C., Eds.; Springer Netherland: Dordrecht, The Netherlands, 2012; pp. 445–458.
41. Kuenzer, C.; Campbell, I.; Roch, M.; Leinenkugel P.; Vo Quoc, T.; Dech, S. Understanding the impacts of hydropower developments in the context of upstream-downstream relations in the Mekong River Basin. *Sustain. Sci.* **2013**, *8*, 565–584.
42. Kummu, M.; Varis, O. Sediment-related impacts due to upstream reservoir trapping of the Lower Mekong River. *Geomorphology* **2007**, *85*, 275–293.
43. Moder, F.; Kuenzer C.; Xu, Z.; Leinenkugel, P.; van Bui, Q. IWRM for the Mekong Basin. In *The Mekong Delta System—Interdisciplinary Analyses of a River Delta*; Renaud, F., Kuenzer, C., Eds.; Springer Netherland: Dordrecht, The Netherlands, 2012; pp. 133–166.

44. Aung, T.T.; Mochida Y.; Than, M.M. Prediction of recovery pathways of cyclone-disturbed mangroves in the Mega delta of Myanmar. *Forest. Ecol. Manag.* **2013**, *293*, 103–113.

45. Islam, G.M.; Islam, A.K.M.; Shopan, A.A. Rahman, M.M.; Lázár, A.N.; Mukhopadhyay, A. Implications of agricultural land use change to ecosystem services in the Ganges delta. *J. Environ. Manag.* **2014**, doi:10.1016/j.jenvman.2014.11.018.
46. Ullmann, T.; Schmitt A.; Roth, A.; Duffe J., Dech S.; Hubberten H.W.; Baumhauer, R. Land cover characterization and classification of arctic tundra environments by means of Polarized Synthetic Aperture X- and C-Band Radar (PolSAR) and Landsat 8 multispectral imagery—Richards Island, Canada. *Remote Sens.* **2014**, *6*, 8565–8593.
47. Slater, J.A.; Garvey, G.; Johnston, C.; Haase, J.; Heady, B.; Kroenung, G.; Little. J. The SRTM data finishing process and products. *Photogramm. Eng. Remote Sens.* **2006**, *72*, 237–247.
48. Lehner, B.; Doell, P. Development and validation of a global database of lakes, reservoirs and wetlands. *J. Hydrol.* **2004**, *296*, 1–22.
49. Carroll, M.L.; Townshend, J.R.; DiMiceli, C.M.; Noojipady, P.; Sohlberg, R.A. A new global raster water mask at 250 m resolution. *Int. J. Digit. Earth* **2009**, *2*, 291–308.
50. Verpoorter, C.; Kutser, T.; Seekell, D.A.; Tranvikm L.J. A global inventory of lakes based on high-resolution satellite imagery. *Geophys. Res. Lett.* **2014**, *41*, 1–7.
51. Vermote, E.F.; Vermeulen, A. Algorithm Technical Background Document Atmospheric Correction Algorithm: Spectral Reflectances (MOD09). Available online: http://modis.gsfc.nasa.gov/data/atbd/atbd_mod08.pdf (accessed on 7 September 2011)
52. Klein, I.; Dietz, A.; Gessner, U.; Kuenzer, C. Global WaterPack: Intra-annual assessment of spatio-temporal variability of inland water bodies. In *Remote Sensing Time Series: Revealing Land Surface Dynamics*; Kuenzer, C., Dech, S., Wagner, W., Eds.; Springer Netherland: Dordrecht, The Netherlands 2015; pp. 99–119.
53. Riggs, G.A.; Hall, D.K.; Salomonson, V.V. *MODIS Snow Products User Guide to Collection 5*; National Snow and Ice Data Center: Boulder, CO, USA, 2006.
54. CGIAR. Available online: http://www.cgiar-csi.org/data/srtm-90m-digital-elevation-database-v4–1 (accessed on 7 April 2015).
55. Sheng, Y.; Su, Y.X.Q. Challenging the cloud contamination problem in flood monitoring with NOAA/AVHRR imagery. *Photogramm. Eng. Remote Sens.* **1998**, *64*, 191–198.
56. Gao, B. NDWI: A normalized difference water index for remote sensing of vegetation liquid water from space. *Remote Sens. Environ.* **1996**, *58*, 257–266.
57. Ji, L.; Zhang, L.; Wylie, B. Analysis of dynamic thresholds for the normalized difference water index. *Photogramm. Eng. Remote Sens.* **2009**, *75*, 1307–1317.
58. McFeeters, S.K. The use of the Normalized Difference Water Index (NDWI) in the delineation of open water features. *Int. J. Remote Sens*. **1996**, *17*, 1425–1432.
59. Xu, H. Modification of Normalised Difference Water Index (NDWI) to enhance open water features in remotely sensed imagery. *Int. J. Remote Sens.* **2006**, *27*, 3025–3033.
60. Feyisa, G.L.; Meilby, H.; Fensholt, R.; Proud, S.R. Automated water extraction index: A new technique for surface water mapping using Landsat imagery. *Remote Sens. Environ.* **2014**, *140*, 23–35.

61. Ryu, J.-H.; Won, J.-S.; Min, K.D. Waterline extraction from Landsat TM data in a tidal flat: A Case study in Gomso Bay, Korea. *Remote Sens. Environ.* **2002**, *83*. 442–456.
62. Klein, I.; Dietz, A.; Gessner, U.; Dech, S.; Kuenzer, C. Results of the Global WaterPack: A novel product to assess inland water body dynamics on a daily basis. *Remote Sens. Lett.* **2015**, *6*, 78–87.
63. Vermote, E.F.; Kotchenova, S. Atmospheric correction for the monitoring of land surfaces. *J. Geophys. Res.* **2008**, *113*, doi:10.1029/2007JD009662.
64. McCullough, I.M.; Loftin, C.S.; Sader, S.A. High-frequency remote monitoring of large lakes with MODIS 500 m imagery. *Remote Sens. Environ.* **2012**, *124*, 234–241.
65. Niu, Z.G.; Gong, P.; Cheng, X.; Guo, J.H. Wang, L.; Huang, H.B.; Shen, S.Q.; Wu, Y.Z.; Wang, X.F.; Wang, X.W.; *et al*. Geographical characteristics of China's wetlands derived from remotely sensed data. *Sci. China Ser. D* **2009**, *52*, 723–738.
66. Vo, Q.T.; Kuenzer, C.; Oppelt, N. How remote sensing supports mangrove ecosystem service valuation: A case study in Ca Mau Province, Vietnam. *Ecosyst. Serv.* **2015**, *14*, 67–75.
67. Vo, Q.T.; Oppelt, Kuenzer, C. Remote sensing in mapping mangrove ecosystems—An object-based approach. *Remote Sens.* **2013**, *5*, 183–201.
68. Hill, P.; Hequette, A.; Ruz, M.; Jenner, K. *Geological Investigations of the Canadian Beaufort Sea Coast*; Open File 2387 of Natural Resources Canada; Geological Survey of Canada: Dartmouth, NS, Canada, 1991; p. 365.
69. Burn, C.R.; Kokelj, S.V. The environment and permafrost of the Mackenzie Delta Area. *Permafr. Periglac. Process.* **2009**, *20*, 83–105.
70. Kuenzer, C.; Bluemel, A.; Gebhardt, S.; Vo Quoc, T.; Dech, S. Remote sensing of mangrove ecosystems: A review. *Remote Sens*. **2011**, *3*, 878–928.
71. Wang, H.; Yang, Z.; Bi, N.; Li, H. Rapid shifts of the river plume pathway off the Huanghe (Yellow) River mouth in response to water-sediment regulation scheme in 2005. *Chin. Sci. Bull*. **2005**, *50*, 2878–2884.
72. Ogilvie, A.; Belaud, G.; Delenne, C.; Bailly, J.S.; Bader, J.C.; Oleksiak, A.; Ferry, L.; Martin, D. Decadal monitoring of the Niger Inner Delta flood dynamics using MODIS optical data. *J. Hydrol*. **2015**, *523*, 368–383.
73. Crétaux, J.; Bergen-Nguyen, M.; Leblan74c, M.; Del Rio Abarca, R.; Delclaux, F.; Mognard, N.; Lion, C.; Pandey, R.K.; Tweed, S.; *et al*. Flood mapping inferred from remote sensing data. *Int. Water Technol. J.* **2011**, *1*, 46–58.
74. Leauthaud, C.; Belaud, G.; Duvail, S.; Moussa, R.; Grünberger, O.; Albergel, J. Characterizing floods in the poorly gauged wetlands of the Tana River Delta, Kenya, using a water balance model and satellite data. *Hydrol. Earth Syst. Sci.* **2013**, *17*, 3059–3075.